

Rapid *in situ* alloying of CoCrFeMnNi high-entropy alloy from elemental feedstock toward high-throughput synthesis via laser powder bed fusion

Bowen WANG^{a,b,c}, Bingheng LU (✉)^{a,b,c}, Lijuan ZHANG (✉)^{b,c}, Jianxun ZHANG^{c,d}, Bobo LI^{a,b,c}, Qianyu JI^{a,b,c}, Peng LUO^{b,e}, Qian LIU^{a,b,c}

^a School of Mechanical Engineering, Xi'an Jiaotong University, Xi'an 710049, China

^b State Key Laboratory of Manufacturing Systems Engineering, Xi'an Jiaotong University, Xi'an 710049, China

^c National Innovation Institute of Additive Manufacturing, Xi'an 710300, China

^d State Key Laboratory for Mechanical Behavior of Materials, Xi'an Jiaotong University, Xi'an 710049, China

^e Institute of Materials, China Academy of Engineering Physics, Mianyang 621908, China

✉ Corresponding author. E-mails: bhlu@mail.xjtu.edu.cn (Bingheng LU); lz201709@126.com (Lijuan ZHANG)

© Higher Education Press 2023

ABSTRACT High-entropy alloys (HEAs) are considered alternatives to traditional structural materials because of their superior mechanical, physical, and chemical properties. However, alloy composition combinations are too numerous to explore. Finding a rapid synthesis method to accelerate the development of HEA bulks is imperative. Existing *in situ* synthesis methods based on additive manufacturing are insufficient for efficiently controlling the uniformity and accuracy of components. In this work, laser powder bed fusion (L-PBF) is adopted for the *in situ* synthesis of equiatomic CoCrFeMnNi HEA from elemental powder mixtures. High composition accuracy is achieved in parallel with ensuring internal density. The L-PBF-based process parameters are optimized; and two different methods, namely, a multi-melting process and homogenization heat treatment, are adopted to address the problem of incompletely melted Cr particles in the single-melted samples. X-ray diffraction indicates that HEA microstructure can be obtained from elemental powders via L-PBF. In the triple-melted samples, a strong crystallographic texture can be observed through electron backscatter diffraction, with a maximum polar density of 9.92 and a high ultimate tensile strength (UTS) of (735.3 ± 14.1) MPa. The homogenization heat-treated samples appear more like coarse equiaxed grains, with a UTS of (650.8 ± 16.1) MPa and an elongation of (40.2% ± 1.3%). Cellular substructures are also observed in the triple-melted samples, but not in the homogenization heat-treated samples. The differences in mechanical properties primarily originate from the changes in strengthening mechanism. The even and flat fractographic morphologies of the homogenization heat-treated samples represent a more uniform internal microstructure that is different from the complex morphologies of the triple-melted samples. Relative to the multi-melted samples, the homogenization heat-treated samples exhibit better processability, with a smaller composition deviation, i.e., ≤ 0.32 at.%. The two methods presented in this study are expected to have considerable potential for developing HEAs with high composition accuracy and composition flexibility.

KEYWORDS laser powder bed fusion (L-PBF), *in situ* alloying, high-entropy alloys, heat treatment, rapid synthesis

1 Introduction

As a newly emerging material, high-entropy alloys (HEAs) exhibit their own mechanical, physical, and chemical properties; and they have elicited attention from academia and industries [1–4]. In contrast with conventional alloys that contain a single primary element and

minor alloying elements for modifying properties, HEAs are composed of five or more primary elements that are mixed in equal or nearly equal atomic element ratios. The formation of disordered single-phase solid solutions with simple crystal structures instead of complex multiphase structures can be realized due to the high configuration entropy in HEAs [5,6]. However, HEAs can exhibit remarkable mechanical properties at high temperatures and considerably better strength, ductility, fracture

toughness, superparamagnetic properties, superconductivity, and irradiation resistance at cryogenic temperatures only with the appropriate combination of elements and regulated proportions [7]. The concentration of each element varies between 5 and 35 at.% in accordance with the definition of Yeh et al. [8]. Therefore, the number of composition combinations for HEAs can be as huge as millions, making HEAs formidable to explore. Accordingly, devising fast synthesis methods to accelerate the development of HEAs as structural materials is imperative. The film-based method and the diffusion multiple method are currently the most commonly used rapid synthesis methods; however, they are unsuitable for fabricating HEA bulks due to size and efficiency limits [9–11].

Additive manufacturing (AM) is an emerging and ever-developing technology wherein solid parts are formed by accumulating materials layer-by-layer. In contrast with traditional cutting technology, AM is a “bottom-up” manufacturing method [12–15]. AM processes have been widely applied to produce HEA bulks from pre-alloyed powder, and these bulks always exhibit uniform composition distribution and excellent performance [16–18]. Zhao et al. [19] doped interstitial N atoms into the matrix of CoCrFeMnNi HEA via reactive atmosphere laser powder bed fusion (L-PBF) in 50% N mixed with Ar gas. The N-doped HEA simultaneously exhibits improved strength and ductility, effectively alleviating the trade-off between strength and ductility. The mainstream AM of HEA bulks from pre-alloyed powder is a gas-atomized method. However, such process of pre-alloyed powders is costly, time-consuming, and lack flexibility in composition. An extensive literature survey showed that using elemental powder mixture as feedstock and *in situ* alloying in a melting pool can make changing the material composition an easy task. On the basis of this method, the design and synthesis of HEAs will be more cost-effective and time-saving [20]. Laser metal deposition (LMD) is capable of producing functionally graded HEAs through the *in situ* alloying of elemental powders [9]. Al_xCrCuFeNi HEA has been *in situ* alloyed via LMD from a blend of elemental powders in the form of a composition gradient [21]. As Al content increases, the microstructure gradually changes from a face-centered cubic (FCC)-based structure to a body-centered cubic-based structure. However, Al content does not change linearly, as expected. Haase et al. [22] prepared an equiatomic CoCrFeMnNi HEA from blended elemental powders via LMD without providing the chemical compositions in the as-built structures. Although the LMD-produced alloy achieved full density and a pronounced texture, some unmolten Cr particles were embedded into the matrix due to the large discrepancies between the melting points of Cr (1907 °C) and other elements (1495 °C for Co, 1538 °C for Fe, 1244 °C for Mn, and 1453 °C for Ni). Melia et al. [23] utilized *in situ* alloying and

compositional grading to rapidly produce a MoNbTaW HEA system via LMD. However, macroscopic pores and unmolten powder particles were observed in most specifications. These pores and particles were created by using constant process parameters instead of optimized parameters for each component. In addition, the chemical composition of most specimens at the macroscale was inconsistent with the prescribed powder flow rate calibration curves. Mo and W were within ±5 at.%, while Nb and Ta were within ±10 at.% around their targeted compositions. Evidently, although the LMD *in situ* alloying of HEAs is the mainstream method, it still suffers from the following problems:

- 1) For elements with high melting temperature, unmolten powder particles are embedded into the matrix;
- 2) The composition of as-built parts is prone to deviate from the expected results;
- 3) Only one set of process parameters is used in fabricating all different components, resulting in mismatch with the specifics.

In this aspect, L-PBF is apparently able to improve the situation. Chen et al. [24,25] *in situ*-alloyed equiatomic CoCrFeMnNi HEA via L-PBF from a blend of CoCrFeNi pre-alloyed powder and Mn elemental powder. However, they did not address the three aforementioned difficulties. In L-PBF, blended elemental powders are pre-spread on a building platform by a recoater, and thus, higher composition accuracy can be obtained. The problem with the inhomogeneous distribution of elementals can be solved by optimizing the alloying process. However, relevant research is still highly limited, and further exploration is necessary to verify the effectiveness of L-PBF-based *in situ* alloying.

To verify whether L-PBF is feasible for the *in situ* synthesis of homogeneous HEA from a blend of elemental powders, the current study selected CoCrFeMnNi HEA, which involved various thermal properties and morphological differences, as the model. Process parameters were optimized, and the composition uniformity and accuracy of the specimens prepared using the optimal process parameters were characterized. Direct and indirect homogeneous syntheses were proposed to solve the problem of unmolten Cr particles embedded into the matrix. The microstructure and performance of the specimens prepared using the two methods were compared.

2 Materials and methods

2.1 Elemental powders and mixture preparation

The mixture used in this study consisted of five elemental powders (Co, Cr, Fe, Mn, and Ni), with purity higher than 99.5% each. Spherical pure Co, Cr, Fe, and Ni powders were gas-atomized with a particle size of 15–53 μm. The

irregularly shaped pure Mn powder was obtained through a fracturing method with a particle size of 15–53 μm . The morphologies of each elemental powder were presented in Fig. 1. The size distributions of each elemental powder are summarized in Table 1, provided by a laser diffraction particle size analyzer (Helos-Rodos).

Each pure elemental powder was weighed in terms of equal atomic ratio. Dry mixing was performed on a horizontal blending machine for 30 h to achieve

homogeneity. To avoid mechanical alloying, a powder mixture was mixed at a speed of 100 r/min, with a ball-to-powder weight ratio of 1:2 and a ball diameter of 5 mm. The container was sealed in an Ar atmosphere glove box to avoid powder oxidation during the mixing process. The morphologies of the prepared elemental powder mixture are shown in Fig. 2(a). The corresponding energy-dispersive X-ray spectroscopy (EDS) mapping result are presented in Fig. 2(b), where purple, red, blue, green, and

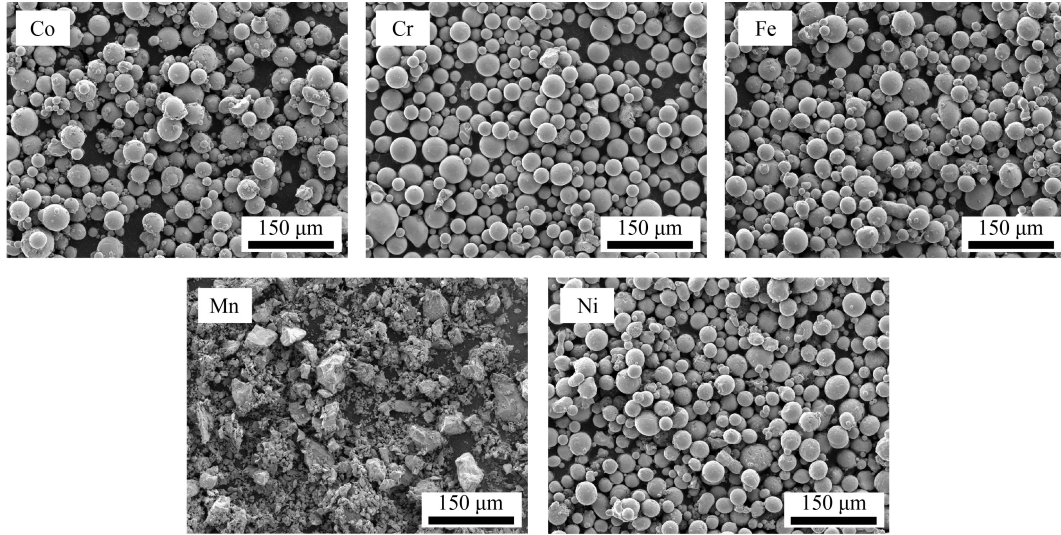


Fig. 1 Secondary electron micrographs of the different morphologies of the used powders.

Table 1 Particle size distributions of the Co, Cr, Fe, Mn, and Ni elemental powders and the blended powder

Powder element	D10/ μm	D50/ μm	D90/ μm	Average diameter/ μm
Co	20.61 ± 0.48	38.71 ± 0.08	59.16 ± 0.06	39.44
Cr	25.31 ± 0.27	41.84 ± 0.21	62.76 ± 0.09	43.13
Fe	24.25 ± 0.02	39.96 ± 0.04	59.32 ± 0.02	41.13
Mn	4.20 ± 0.03	24.48 ± 0.02	65.44 ± 0.46	30.27
Ni	25.08 ± 0.30	39.90 ± 0.01	58.98 ± 0.10	41.17
Blended powder	14.28 ± 0.18	38.21 ± 0.14	61.67 ± 0.53	38.61

Notes: D10, D50, and D90 represent the volume content of particles smaller than this size accounts for 10%, 50%, and 90% of all particles, respectively.

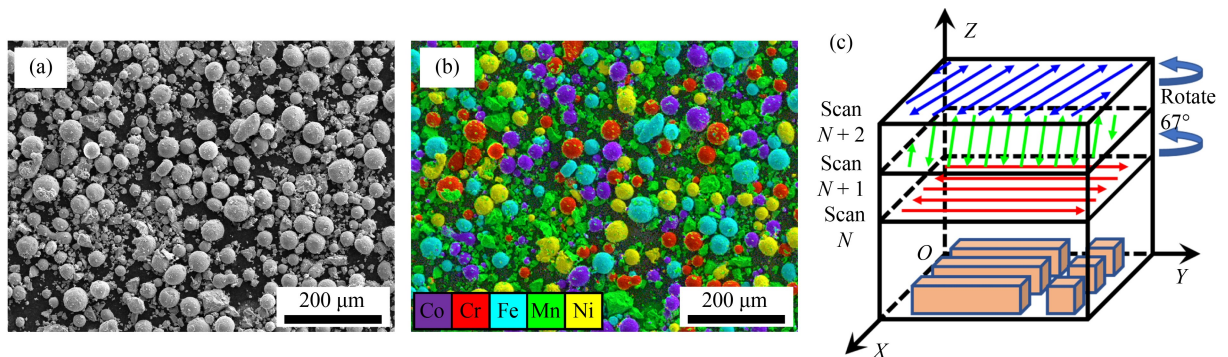


Fig. 2 (a) Morphologies of the prepared elemental powder mixtures, (b) energy-dispersive X-ray spectroscopy mapping, and (c) forming strategy.

yellow represent Co, Cr, Fe, Mn, and Ni, respectively. After mixing well, each elemental powder was evenly distributed in the mixture, with no powder agglomeration observed. The spherical shape was preserved in the Co, Cr, Fe, and Ni particles, maintaining the flowability of the powder mixture. The Mn particles with irregular shape were also mixed uniformly with the other elemental particles. The size distribution of the blended powder was also analyzed and listed in Table 1. The chemical compositions of the mixture in the *in situ*-alloyed HEAs are listed in Table 2. The compositions were determined via inductively coupled plasma mass spectrometry (ICP-MS; NexION 350D). The deviations of the chemical concentrations of the five component elements was less than 0.18 at.% from the nominal equimolar concentrations. Such value was acceptable.

2.2 Sample preparation

A commercial BLT-S200 L-PBF machine (China) was used in this study. It was equipped with a 400 W fiber laser (1070 nm wavelength) with a focal beam diameter of 100 μm . To minimize oxidation, high-purity Ar was used to purge the building chamber, and the O content was maintained at below 100 ppm (1 ppm = 0.0001%) during processing. Some cubic samples, 8 mm \times 8 mm \times 8 mm, were prepared at the inception to obtain the optimal parameters as the benchmark. The process parameters listed in Table 3 were selected on the basis of a previous research [16]. For all the samples, the laser power (P) was 280 W, the hatch spacing (h) was 90 μm , and the layer thickness (t) was 40 μm . The scanning speed (v) was varied from 470 to 970 mm/s to obtain diverse volumetric energy density (VED), which was defined as follows [26]:

$$\text{VED} = \frac{P}{vht}. \quad (1)$$

Laser scanning was performed in zigzag pattern, rotating by 67° each scanning, as shown in Fig. 2(c).

Notably, a uniform composition and a dense structure cannot be obtained by optimizing only the process parameters (see Section 3.1). To fabricate fully dense and uniformly structured samples, a multi-melting process and homogenization heat treatment are necessary. Among the six cubic samples, the one that is fully dense and has a minimum content of unmolten Cr particles is called the single-melted sample. Its process parameters were selected as the base parameters. To address the problem of unmelted particles, the current study used two different methods: a multi-melting process and homogenization heat treatment. By using the base parameters, remelting was performed layer by layer once, two times, and three times. The corresponding samples were called double-, triple-, and quadruple-melted samples, respectively. Homogenization heat treatment was performed on the single-melted samples for 5 h at 1250 °C in a vacuum furnace, followed by furnace cooling. The treated samples are called homogenization samples.

2.3 Material microstructure characterization

To identify the crystal structure of the blended powder and the *in situ*-alloyed samples, X-ray diffraction analysis (XRD; Bruker D8 Advanced A25, Cu K α radiation) was conducted, with a scanning step size of 0.02°, and ranging from 20° to 100°. To reveal the microstructure of the *in situ*-alloyed HEA, samples were grounded with SiC abrasive papers and then polished with 1 μm diamond suspension. Microstructure and chemical composition

Table 2 Inductively coupled plasma analysis results of the raw materials used in this study and the chemical composition of the *in situ*-synthesized CoCrFeMnNi HEA samples via different L-PBF sequences

Samples	Blended powder/at. %	Triple-melted sample/at. %	Homogenization heat-treated sample/at. %
Co	20.00 \pm 0.15	21.18 \pm 0.26	19.80 \pm 0.18
Cr	20.13 \pm 0.25	21.18 \pm 0.35	20.32 \pm 0.36
Fe	20.02 \pm 0.25	21.16 \pm 0.28	20.22 \pm 0.31
Mn	20.03 \pm 0.18	16.40 \pm 0.24	19.93 \pm 0.25
Ni	19.82 \pm 0.18	20.39 \pm 0.19	19.72 \pm 0.21

Table 3 Process parameters used in this study

No.	Laser power/W	Scanning speed/(mm·s ⁻¹)	Hatch distance/ μm	Layer thickness/ μm	VED/(J·mm ⁻³)
1	280	970	90	40	80
2	280	870	90	40	89
3	280	770	90	40	101
4	280	670	90	40	116
5	280	570	90	40	136
6	280	470	90	40	165

distribution were investigated via scanning electron microscopy (SEM) by using JEOL JSM-7900F, which was equipped with an energy-dispersive spectrometer (Oxford Instruments X-Max SDD) and an electron backscatter diffraction (EBSD) detector (Oxford Nordlys-CMOS detector). EBSD analysis required the polished samples to be processed further to eliminate the stress layer. This procedure was performed for 60 min on an ion polishing instrument (Leica EM RES102) at 5 kV and an inclination of 10° . The step size of EBSD was set to 1 μm , and the smallest recognizable grain was 10 pixels in area. EBSD data were analyzed using Channel 5 software.

Transmission electron microscopy (TEM; Talos-F200) was used to observe the sub-microstructures at an acceleration voltage of 200 kV. The TEM samples were prepared on a twin-jet electro-thinning device (Denmark Struers A/S). The tensile test was performed on a universal material testing machine (Instron 5982) under quasistatic loading at a strain rate of $10^{-3}/\text{s}$ at room temperature. Strain was measured directly on the samples by using a noncontact video extensometer (AVE2). Yield strength (YS) values were the proof stresses at 0.2% deformation. Dog bone-shaped specimens were cut from the *in situ*-alloyed HEA bulks, with a rectangular cross

section of 5 mm \times 3 mm and a gauge length of 20 mm. Then, the fracture surfaces were observed via SEM.

3 Results and discussion

3.1 Processing development

The optical micrographs for the single-melted samples prepared from a mixture of elemental powders under different VEDs are shown in Fig. 3. For each specimen, a cross-sectioned surface was cut along the building direction and then polished. Incompletely melted particles and pores could be observed and marked by red arrows. Incompletely melted particles were Cr particles, which were also characterized in Section 3.2. Evidently, the number and size of partially melted Cr particles decreased significantly as VED increased, improving the homogeneity of the alloys. The morphology of pores also varied with VED. In case of low VED (80 J/mm³, Fig. 3(a)), some pores were present in the samples, along with a large number of incompletely melted Cr particles, due to input energy deficiency and incomplete melting [27]. When energy density was increased from 89 to 101 to 116 J/mm³ (Figs. 3(b)–3(d)), a dense structure was

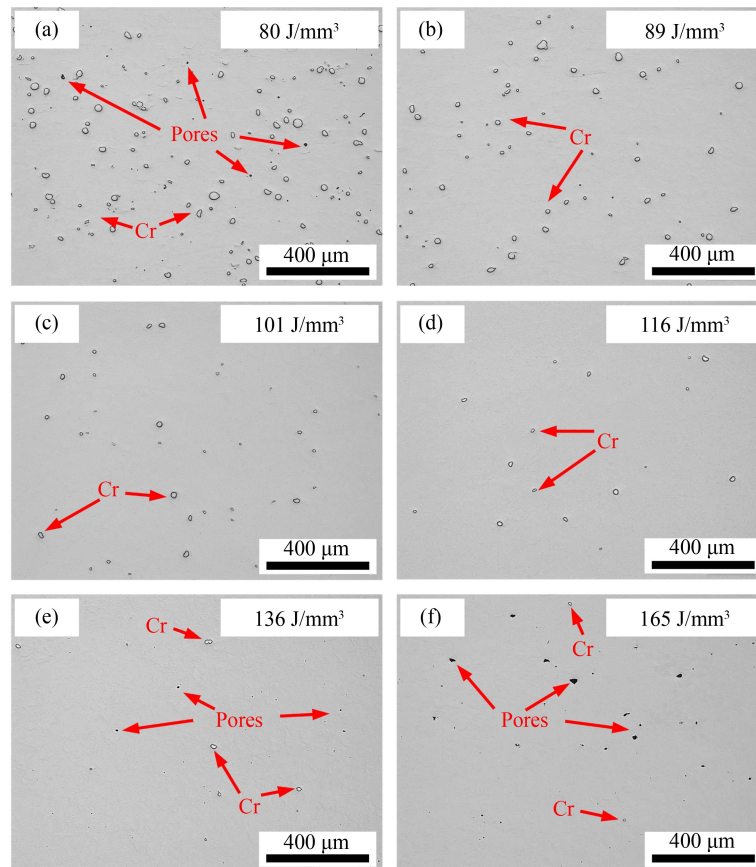


Fig. 3 Longitudinal section optical micrographs of as-built single-melted samples at VEDs of (a) 80 J/mm³, (b) 89 J/mm³, (c) 101 J/mm³, (d) 116 J/mm³, (e) 136 J/mm³, and (f) 165 J/mm³.

obtained. Some Cr particles were melted during the L-PBF process, and thus, the number and size of unmelted Cr particles decreased with an increase in VED. However, when VED was too high, i.e., 136 and 165 J/mm³ (Figs. 3(e) and 3(f)), more pores were present because the melting pool was overheated and the material tended to evaporate [28]. In the samples formed at an energy density of 165 J/mm³, a large number of pores were observed, with a few unmelted Cr particles.

More pores would appear at high energy density, worsening the density and structure, although the dissolution degree of Cr particles could be improved. Therefore, improving the uniformity of Cr should be in parallel with ensuring internal density. Without impairing internal density, energy density should be set as high as possible and the processing parameters were chosen as the basis for the subsequent process research. Thus, set No. 4 (laser power: 280 W, scanning speed: 670 mm/s, hatch space: 90 μm, layer thickness: 40 μm, and VED: 116 J/mm³) was selected as the base process parameters. Two different methods, namely, a multi-melting process and homogenization heat treatment, were adopted to solve the problem of incompletely melted Cr particles in parallel with a dense internal structure.

Figure 4 shows the longitudinal section optical micrographs of the single-, double-, triple-, and quadruple-melted samples. By using the same base parameters, each layer was melted once or more than once, with a rotation of 67° for each scanning. For example, during the double-melting sequence, each layer was melted two times. The second melting and solidification sequence was performed without adding powder after the first melting sequence. The base parameters were used, with the scanning direction rotated by 67°.

As shown in Figs. 4(a)–4(c), the size and number of unmelted Cr particles decreased remarkably after multi-melting was implemented, because the larger the number of remelting, the longer the time for particles to dissolve. The dense structure can be preserved after single-, double-, and triple-melting sequences; however, a large number of pores appeared in the samples after the quadruple melting sequence, as shown in Fig. 4(d). Evidently, prolonged heat accumulation during quadruple melting leads to overheating of the melting pool and the evaporation of materials, forming pores in the matrix. Nonetheless, multiple melting of the same layer can lead to successive melting and solidification events and improve the uniformity of the bulk composition, similar to the arc melting method, wherein the material is melted several times to improve homogenization [29]. To dissolve the residual Cr particles into the matrix, homogenization heat treatment method was also applied as an alternative to the single-melted samples. The single-melted samples were homogenized via heat treatment at 1250 °C for 5 h, and the uniformity of composition was achieved via element diffusion. Chemical homogeneity and accuracy were discussed in Section 3.2.

In the current study, three samples that were created via single melting, triple melting, and single melting plus homogenization heat treatment were selected, and their microstructure and properties were characterized and analyzed.

3.2 Characterization of composition homogeneity and accuracy

The homogeneity of elemental distribution is a critical issue in the *in situ* synthesis of HEAs. The SEM and EDS

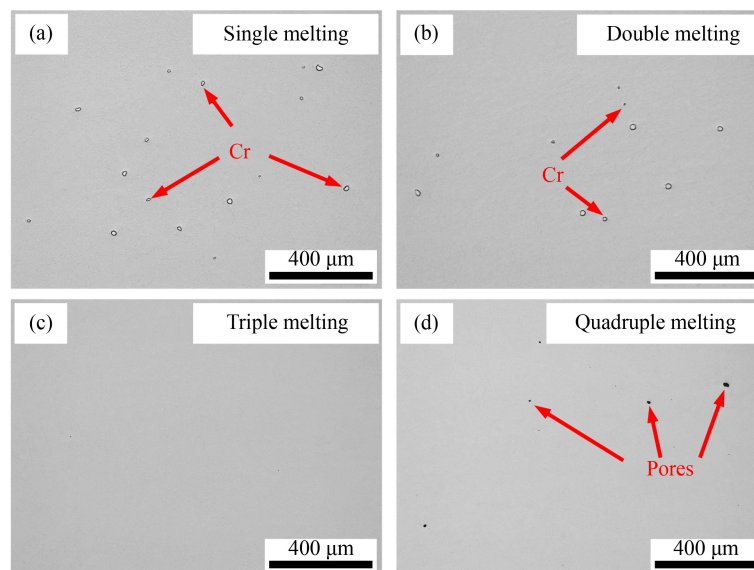


Fig. 4 Longitudinal section optical micrographs of *in situ*-alloyed CoCrFeMnNi HEA with different numbers of melting steps: (a) single melting, (b) double melting, (c) triple melting, and (d) quadruple melting.

mapping of the *in situ*-synthesized CoCrFeMnNi HEA from elemental powders are shown in Fig. 5. The SEM and EDS mapping of the single-melted samples are

presented in Fig. 5(a). The undissolved Cr particles were observed to scatter randomly, indicating that the partially melted particles mentioned in Section 3.1 are Cr particles.

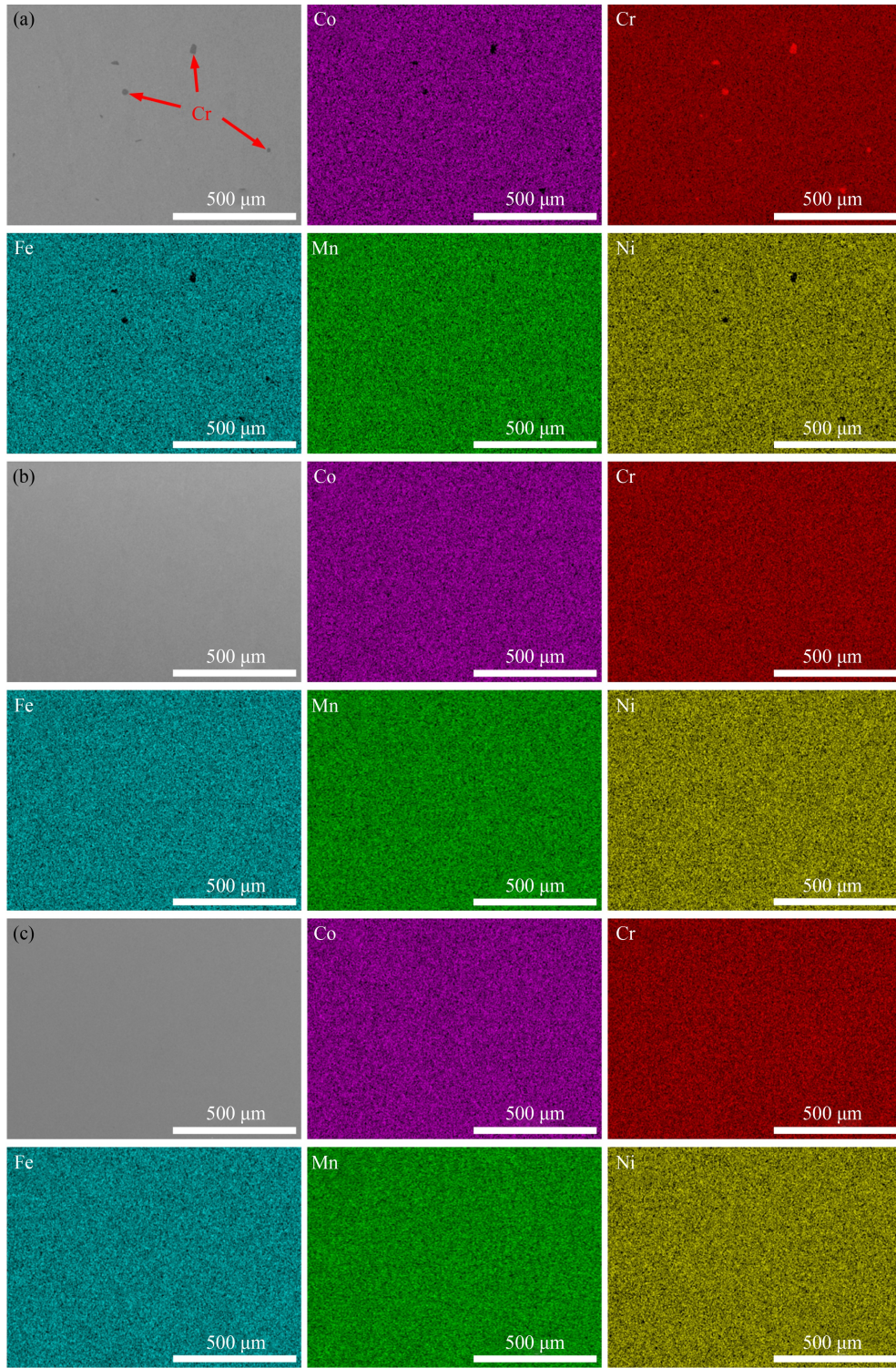


Fig. 5 Scanning electron microscopy and energy-dispersive X-ray spectroscopy mapping of the *in situ*-synthesized CoCrFeMnNi high-entropy alloy from elemental powders through different processes: (a) single-melted samples (laser power: 280 W, scanning speed: 670 mm/s, hatch space: 90 μm, layer thickness: 40 μm, and VED: 116 J/mm³), (b) triple-melted samples, and (c) single-melted + homogenization heat-treated samples.

Only large Cr particles dissolved incompletely during the single melting process, which was most likely due to the fact that Cr has the highest melting point, i.e., 1907 °C, among the elemental powders used in the mixture (Co: 1495 °C, Fe: 1538 °C, Mn: 1244 °C, and Ni: 1453 °C) [30]. The powder in the L-PBF process went through a rapid melting and solidifying process (10^5 – 10^8 K/s) [31,32] within an extremely short time. This phenomenon could limit the diffusion of Cr into the molten pool. Moreover, the EDS element mapping revealed that, except for Cr, the four other principal elements were distributed evenly. This improvement in the mixing uniformity of each element was ascribed to the intense convection flow in the molten pool and the partial remelting of the previous layers during L-PBF [33].

Triple-melted specimens were determined to be homogeneous. As illustrated in Fig. 5(b), the internal structure was dense, without pores, and had no undissolved elemental powders. The chemical homogeneity of specimens was also verified via EDS measurements. The elements Co, Cr, Fe, Mn, and Ni were distributed evenly. Thus, increasing the time of melting can promote the uniformity of element distribution. In summary, increasing the number of melting increases the molten state time interval of the alloy, providing a longer time sufficient for Cr particles to dissolve and diffuse [34,35]. By contrast, the rapid solidification in each scanning will considerably inhibit the segregation of elements and promote the uniformity of element distribution.

Homogenization heat treatment was performed to improve the composition uniformity of the single-melted samples [36,37]. All the elements (Co, Cr, Fe, Mn, and Ni) were uniformly distributed, as shown in Fig. 5(c). Homogenization heat treatment considerably promoted the diffusion of Cr into the matrix, enhancing the

chemical uniformity of the single-melted samples. In the samples prepared via L-PBF, hierarchical structures, including melting pool boundaries, columnar grains, submicron cellular structures, and dislocations, were commonly found [38,39]. In addition, the unmelted Cr particles demonstrated good interface contact with the matrix. Therefore, when heat treatment temperature is greater than 0.9 times the melting point temperature, the two factors will further accelerate the dissolution of unmelted Cr particles into the matrix, eventually realizing a homogeneous composition.

For element composition accuracy analysis, ICP analysis was conducted, and the results are listed in Table 2. Among the five elements, only Mn exhibited remarkable deviation in the triple-melted samples, indicating the loss of Mn during L-PBF; such phenomenon is commonly encountered in L-PBF, because Mn has the lowest boiling point and the smallest vaporization heat [26]. Moreover, the burning loss of Mn was aggravated by the triple remelting sequence to ~3.6 at.%. This deviation in composition accuracy can be eliminated by increasing the content of Mn powders in raw materials. An equivalent element concentration was obtained in the homogenization heat-treated specimens (applied to single-melted samples) compared with the elemental powder mixture. Therefore, high elemental accuracy and homogenization could be achieved simultaneously via homogenization heat treatment.

3.3 Phase analysis

Figure 6 shows the XRD patterns of the initial elemental powder mixtures, single-melted samples, triple-melted samples, and homogenization heat-treated samples, which were extracted from the central region in the YOZ plane,

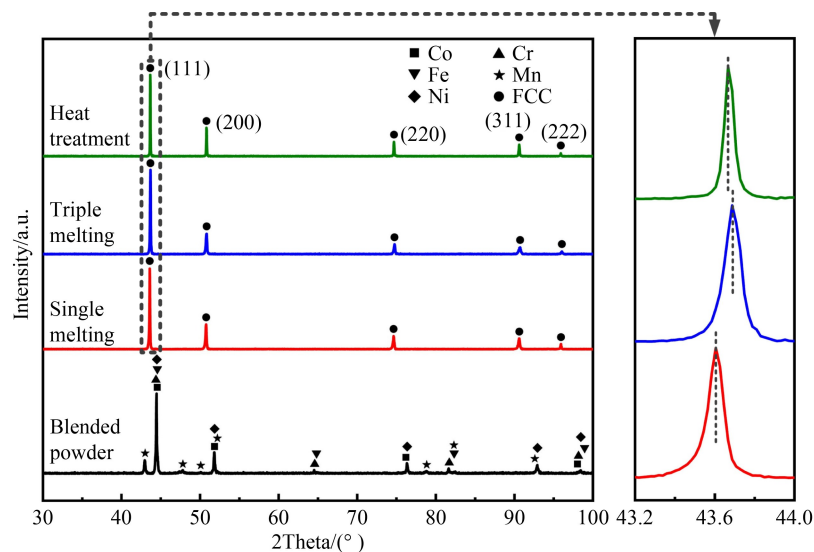


Fig. 6 XRD patterns of the initial elemental powder mixture, single-melted samples, triple-melted samples, and homogenization heat-treated samples, with peak (111) enlarged.

as shown in Fig. 2(c). The XRD patterns revealed the existence of each pure metal powder in the initial elemental powder mixture. After the single-melting sequence, the single pattern of CoCrFeMnNi HEA FCC was indexed, without observing any elemental powder pattern. This finding indicates that by using L-PBF, HEA microstructure can be obtained from elemental powders. The pattern of incompletely melted Cr particles was not found on the spectra, probably due to its low amount and small size. The triple-melted samples and homogenization heat-treated samples had the same FCC phase as that of the single-melted samples, without a trace of precipitation phase, confirming that the FCC phase was maintained throughout the multi-melting process and homogenization heat treatment. The lattice parameter of the single-melted, triple-melted, and homogenization heat-treated samples was approximately 3.593, 3.589, and 3.592 Å, respectively, which were extremely close to the lattice parameters achieved via arc melting (~3.59 Å) and L-PBF (~3.60 Å) from the pre-alloyed powder [26,40]. Moreover, peak (111) in the triple-melted and homogenization heat-treated samples shifted to a higher two theta value, also indicating a decrease in lattice parameters. As remelting intensified, an increasing number of Mn evaporated, and thus, its content in the samples decreased, leading to declining lattice parameters. In the homogenization heat treatment, however, the reduction of lattice parameters in the samples was due to the fact that a large amount of tensile stress was released during the process.

3.4 Microstructure characterization

Further characterization of grain morphologies and preferred grain growth orientations was conducted via EBSD. The typical EBSD inverse pole figure (IPF) maps are shown in Fig. 7, taken from planes perpendicular to the *X*-, *Y*-, and *Z*-direction. Figure 7(a) illustrates that the typical columnar grain morphology and similar crystallographic orientation characteristics of the single-melted samples are extremely close to those of the samples produced via L-PBF from pre-alloyed powders [16,41]. A columnar crystal structure parallel to the *Z*-direction can be clearly seen in the rebuilt 3D IPF map. Some of the grains were elongated to hundreds of microns long, with a width of only dozens of microns. The average grain size was about 24.1 μm. The formation of the columnar crystal structure was mostly related to the extremely high cooling gradient along the *Z*-direction. In the tiny molten pool produced by the highly concentrated laser, temperature was extremely high. In the solidification process, heat would dissipate rapidly along the substrate, achieving a high cooling rate in favor of rapid solidification. Moreover, under the synergistic effect of epitaxial growth, the columnar crystal structure was formed. In accordance with the corresponding pole

figures (PFs) and IPFs, aggregations of $\langle 110 \rangle$ orientations were dominantly parallel to the *Z*-direction, while aggregations of $\langle 001 \rangle$ orientations were parallel to the *X*-direction. Similar textures for additive manufactured materials were noted previously in the literature. For example, the FCC Ni alloy 718 produced via L-PBF has a characteristically strong $\{110\}$ -type texture along the build direction and a $\{100\}$ texture along the transverse direction [42]. Cellular growth is the dominant solidification mode during L-PBF. Cells grow in directions perpendicular to the molten pool boundary in the $\langle 001 \rangle$ orientation, which is the preferred growth direction in FCC crystals along the maximum heat flux direction. The boundary of the molten pool would have different curvatures at different positions, causing different angles of rotation for the preferred orientation $\langle 001 \rangle$. Thus, a major $\{011\}$ $\langle 100 \rangle$ texture and a minor $\{001\}$ $\langle 100 \rangle$ texture on the *XOY* plane along the *X*-direction were produced.

The results of the EBSD analysis of the triple-melted samples are presented in Fig. 7(b). In the triple-melted samples, large amounts of columnar crystal structure grains along the *Z*-direction were also formed due to the overall highly localized heat input. Compared with the single-melted samples, the width of the columnar grains increased from dozens of microns to hundreds of microns, and the length also increased from hundreds of micrometers to the order of millimeter, indicating that epitaxial growth had penetrated through dozens of layers. The average grain size also increased from about 24.1 to about 29.1 μm. Figure 7(a) clearly shows that the single-melted samples lacked strong crystallographic textures, and their maximum polar density was only 3.97 mud. By contrast, a strong crystallographic texture was observed in the triple-melted samples, as shown in Fig. 7(b), with the maximum polar density increasing to 9.92 mud. Therefore, remelting will not change the rapid solidification nature of L-PBF, although the heat input and substrate temperature increased during triple-melting. However, such increase in heat and temperature could have influence the growth rate and cooling rate, enhancing the elongated grains with strong texture on the basis of previously solidified grains.

The homogenization heat-treated samples were also analyzed via EBSD, as shown in Fig. 7(c). Homogenization heat treatment considerably changed the grain morphologies of the single-melted samples. In contrast with the columnar crystal structure in the single-melted samples and triple-melted samples, the homogenization heat-treated samples had a coarse equiaxed grains structure, with the largest average grain size of 35.9 μm. Furthermore, the texture weakened, with a slight aggregation in the preferential orientation $\{011\}$ $\langle 100 \rangle$ and $\{001\}$ $\langle 100 \rangle$ on the *XOY* plane, and the maximum polar density of 3.42 mud. In the single-melted samples, numerous fine grains with irregular shape existed along

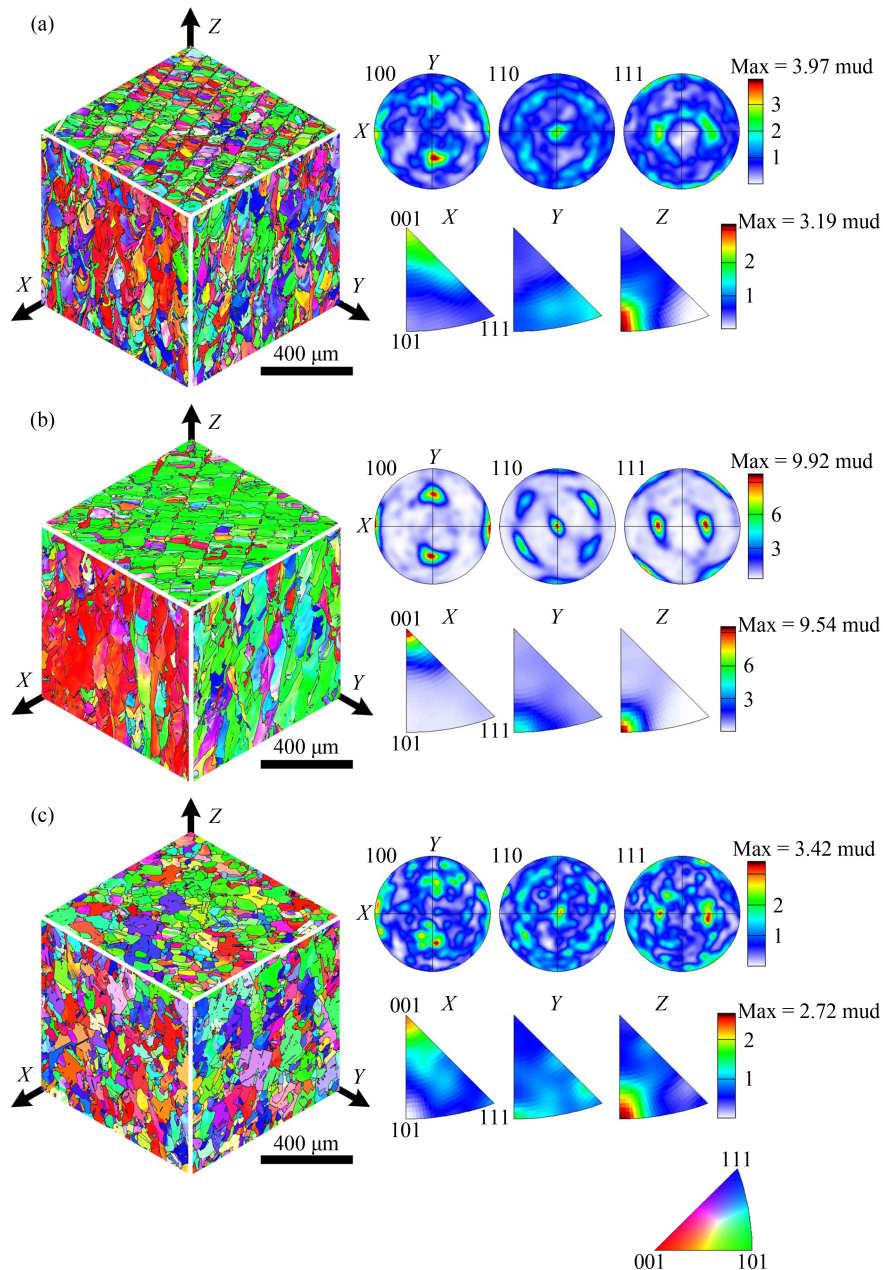


Fig. 7 3D crystallographic orientation demonstration and the corresponding pole figures and inverse pole figures of the (a) single-melted samples, (b) triple-melted samples, and (c) homogenization heat-treated samples (applied to single-melted samples).

the track borders under complex heat transfer condition. These fine grains with random orientation will be easily converted into coarse grains through annealing. Moreover, the original columnar crystal structure is also prone to recrystallize and grow into an equiaxed crystal structure under heating. These factors eventually led to the formation of equiaxed crystals with larger average grain size and the weakening of texture.

3.5 Mechanical properties

The triple-melted samples and homogenization heat-treated samples (applied to single-melted samples)

underwent mechanical tests at room temperature. Their typical engineering stress–strain curves are presented in Fig. 8. The triple-melted samples exhibited excellent mechanical properties, with an UTS of (735.3 ± 14.1) MPa, YS (σ_y) of (610.2 ± 15.8) MPa, and an elongation to failure (ϵ_f) of $14.4\% \pm 0.9\%$. Although the homogenization heat-treated samples had lower strength relative to the triple-melted samples, a UTS of (650.8 ± 16.1) MPa, and σ_y of (293.8 ± 8.1) MPa, they had considerably larger elongation to failure (ϵ_f), i.e., $40.2\% \pm 1.3\%$.

The differences in mechanical properties primarily originate from the changes in strengthening mechanism. Three mechanisms made major contributions to YS (σ_y):

lattice friction stress, grain boundary strengthening related to the Hall–Petch relationship, and dislocation strengthening [39]. σ_y can be expressed as follows:

$$\sigma_y = \sigma_0 + \sigma_{GB} + \sigma_{dis}, \quad (2)$$

where σ_0 is friction stress, σ_{GB} is grain boundary strengthening, and σ_{dis} is strengthened dislocation.

The σ_0 of equiatomic CoCrFeMnNi is 147 MPa [43]. The alloys synthesized using the two methods possess the same lattice friction stress.

The grain boundary can suppress dislocation motion, and thus, average grain size also affects the YS of a metallic material. The effect of grain boundary strengthening, σ_{GB} , can be estimated via Hall–Petch relation and is expressed as

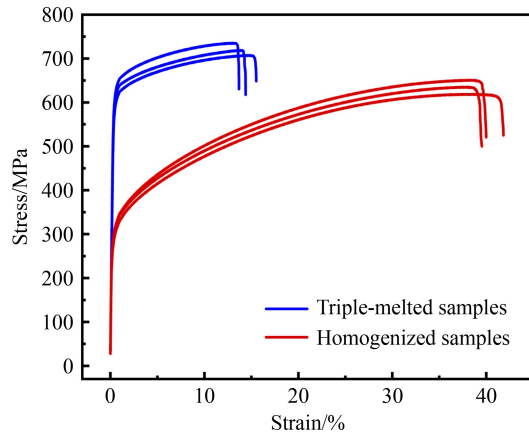


Fig. 8 Engineering tensile stress–strain curves of the triple-melted samples and homogenization heat-treated samples.

Table 4 All strengthening components and estimated YS

Samples	σ_0 /MPa	σ_{GB} /MPa	σ_{dis} /MPa	σ_y /MPa	Estimated YS/MPa	Deviation/%
Triple-melted samples	147	91.6	347.3	585.9	610.2	4.0
Homogenized samples	147	82.4	95.6	325.0	293.8	10.6

Note: Deviation = $\frac{|\text{Estimated YS} - \sigma_y|}{\text{Estimated YS}} \times 100\%$.

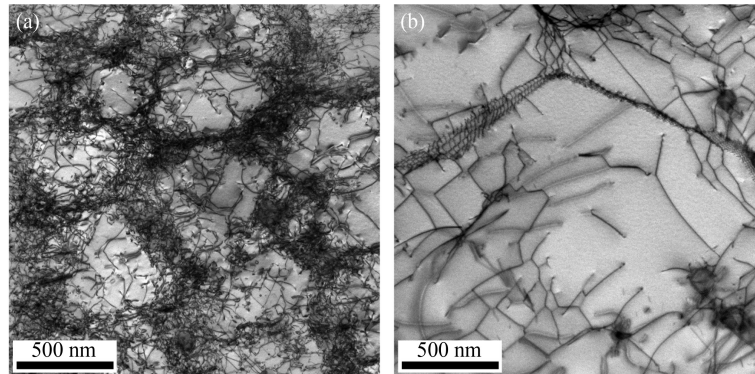


Fig. 9 Transmission electron microscopy bright field images of (a) triple-melted samples with cellular substructures and (b) homogenization heat-treated samples (applied to single-melted samples) without cellular substructures.

$$\sigma_{GB} = k/\sqrt{d}, \quad (3)$$

where k is the strengthening coefficient and d is the average grain size.

Here, the strengthening coefficient is $494 \text{ MPa}\cdot\mu\text{m}^{1/2}$ [43], and the average grain sizes are 29.1 and 35.9 μm . The estimated grain boundary strengthening is 91.6 and 82.4 MPa for the triple-melted and homogenization heat-treated samples, respectively.

Dislocation strengthening, σ_{dis} , is given by Ref. [44] as follows:

$$\sigma_{dis} = MaGb\sqrt{\rho}, \quad (4)$$

where M is the Taylor factor, 3.06; a is a constant, 0.33 [45]; G is the shear modulus, 80.9 GPa [46]; b is the Burgers vector, 0.2536 [47]; and ρ is the dislocation density. The estimated dislocation density of the triple-melted and homogenization heat-treated samples was 2.81×10^{14} and $2.13 \times 10^{13} \text{ m}^{-2}$ via EBSD, respectively. Therefore, the contribution of dislocation strengthening is 347.3 MPa for the triple-melted samples and 95.6 MPa for the homogenization heat-treated samples. The contributions of each strengthening mechanism to the overall predicted strengths are listed in Table 4.

The change in dislocation strengthening effect is the major factor that made YS considerably different between the two samples. To visually observe the change in dislocation density, the dislocation morphologies of the triple-melted samples and the homogenization heat-treated samples (applied to single-melted samples) were characterized via TEM, as shown in Fig. 9.

In the triple-melted samples, the cellular substructures

were observed to be ~500 nm in size, with wall thickness of approximately 80 nm, decorated with dislocations of high density. However, no cellular structures, but some dislocations, were found in the homogenized heat-treated samples. High-density dislocation-decorated cellular structures were formed under solidification conditions during the L-PBF process [48], and this phenomenon could significantly hinder dislocation movement, and thus, improve YS. Although YS decreased because of homogenization heat treatment, UTS did not decrease as much as YS. A similar phenomenon was also observed in Zhu et al. [39], and it is likely due to the increase in elongation at the fracture [49].

The values of tensile property are listed in Table 5 and compared with those of the as-built L-PBF samples produced from pre-alloyed powders and other welding processes in the reported literature. The triple-melted samples had higher UTS and YS values but lower elongation compared with the samples produced from pre-alloyed powders. This result contributed to the remarkable texture formed on the triple-melted samples, as illustrated in the EBSD section. However, compared with the those produced from pre-alloyed powders, the

homogenization heat-treated samples had nearly the same UTS, considerably better elongation, but poorer YS. Nevertheless, the homogenized heat-treated samples are on par with traditional welding materials in terms of YS.

The fractographic morphologies of triple-melted samples and homogenization heat-treated samples are shown in Fig. 10. As illustrated, typical ductility fracture morphology could be observed over the entire fracture surface for both samples. As depicted in Fig. 10(a), some cleavage facets and micron-sized cracks were found in the triple-melted samples, marked by red and white arrows, respectively. The propagation of these weakest positions will accelerate fractures. However, in the homogenization heat-treated samples, no cracks were found in Fig. 10(b), exhibiting relatively flat fracture morphology. Under higher magnification, both samples exhibited the characteristic of typical ductile fracture for uniformly covering small dimple topography on the whole fracture surfaces. The size of dimples in the homogenization heat-treated samples was significantly larger than that in the triple-melted samples, indicating better ductility.

Table 5 Tensile properties of triple-melted samples, homogenization heat-treated samples, and samples produced using other processes

Samples	σ_y /MPa	UTS/MPa	ε_f /%	Reference
Triple-melting samples	610.2 ± 15.8	735.3 ± 14.1	14.4 ± 0.9	Present work
Homogenized samples	293.8 ± 8.1	650.8 ± 16.1	40.2 ± 1.3	Present work
L-PBF samples from pre-alloyed powders	582.9 ± 10.8	679.8 ± 12.9	23.8 ± 1.4	[16]
L-PBF samples from pre-alloyed powders	519.0	601.0	35.0	[26]
LMD samples from pre-alloyed powders	346.0	566.0	26.0	[50]
Electron beam welding samples	320.0	617.0	27.0	[51]
Gas W arc welding samples	297.0	530.0	15.0	[51]

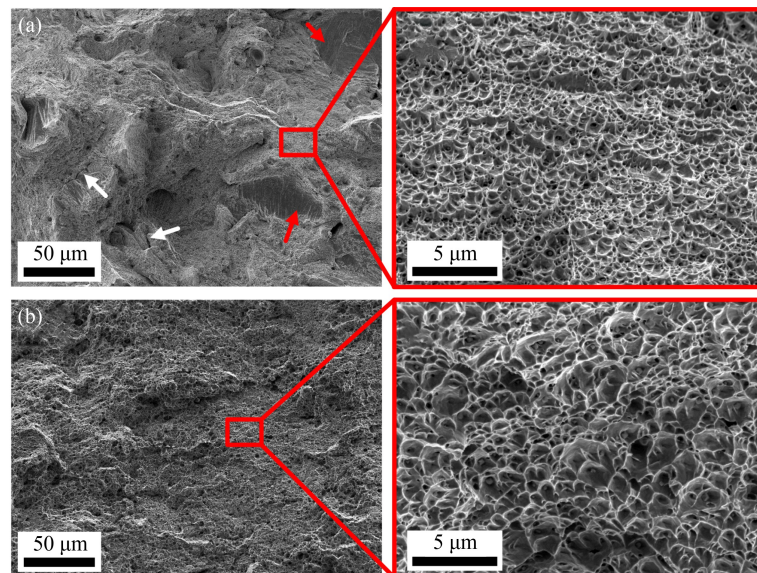


Fig. 10 (a) Tensile fracture surface of the triple-melted samples and (b) homogenization heat-treated samples.

4 Conclusions

This study contributes to the understanding of the *in situ* alloying of elemental powder mixtures via L-PBF. Bulk CoCrFeMnNi HEA was *in situ*-alloyed from the blend of spherical Co, Cr, Fe, and Ni elemental powders and nonspherical Mn elemental powder. Two different methods, namely, multi-melting process and homogenization heat treatment, were adopted to address the problem of unmelted Cr particles in single-melted samples. Homogeneity and compactness were achieved simultaneously. Some conclusions can be drawn as follows:

(1) Chemical homogeneity and dense structure cannot be obtained simultaneously by only optimizing process parameters. Multi-melting or homogenization heat treatment is necessary to achieve uniformity parallel with ensuring internal density. Relative to multi-melting, homogenization heat treatment achieves better processability, with a smaller composition deviation, i.e., < 0.32 at.%.

(2) Large amounts of columnar grains parallel to the Z-direction are found in the triple-melted samples. Strong crystallographic texture can be observed, with a maximum polar density of 9.92 mud. However, the homogenization heat-treated samples have coarse equiaxed grain morphologies with weakened textures.

(3) The triple-melted samples exhibit good mechanical properties, with a UTS of (735.3 ± 14.1) MPa, a YS (σ_y) of (610.2 ± 15.8) MPa, and an elongation to failure (ϵ_f) of $(14.4\% \pm 0.9\%)$. By contrast, the homogenization heat-treated samples have considerably larger elongation (ϵ_f), i.e., $(40.2\% \pm 1.3\%)$, although they have lower strength, i.e., UTS and σ_y of (650.8 ± 16.1) MPa and (293.8 ± 8.1) MPa, respectively.

Nomenclature

Abbreviations

AM	Additive manufacturing
EBSD	Electron backscatter diffraction
EDS	Energy-dispersive X-ray spectroscopy
FCC	Face-centered cubic
HEA	High-entropy alloy
ICP	Inductively coupled plasma
IPF	Inverse pole figure
L-PBF	Laser powder bed fusion
LMD	Laser metal deposition
PF	Pole figure
SEM	Scanning electron microscopy
TEM	Transmission electron microscopy
UTS	Ultimate tensile strength

VED	Volumetric energy density
XRD	X-ray diffraction
YS	Yield strength

Variables

a	A constant
b	Burgers vector
d	Average grain size
G	Shear modulus
h	Hatch spacing
k	Strengthening coefficient
M	Taylor factor
P	Laser power
t	Layer thickness
v	Scanning speed
ρ	Dislocation density
σ_0	Friction stress
σ_{dis}	Strengthened dislocation
σ_{GB}	Grain boundary strengthening
σ_y	Yield strength
ϵ_f	Elongation to failure

Acknowledgements This work was supported by the National Innovation Institute of Additive Manufacturing, China. The authors thanked Chao Li of the Instrument Analysis Center of Xi'an Jiaotong University for conducting field-emission transmission electron microscopy analysis.

Conflicts of Interest The authors declare no conflict of interest.

References

- Zhang Y, Zuo T T, Tang Z, Gao M C, Dahmen K A, Liaw P K, Lu Z P. Microstructures and properties of high-entropy alloys. *Progress in Materials Science*, 2014, 61: 1–93
- Chen S J, Oh H S, Gludovatz B, Kim S J, Park E S, Zhang Z, Ritchie R O, Yu Q. Real-time observations of TRIP-induced ultrahigh strain hardening in a dual-phase CrMnFeCoNi high-entropy alloy. *Nature Communications*, 2020, 11(1): 826
- Li W D, Xie D, Li D Y, Zhang Y, Gao Y F, Liaw P K. Mechanical behavior of high-entropy alloys. *Progress in Materials Science*, 2021, 118: 100777
- Moghaddam A O, Shaburova N A, Samodurova M N, Abdollahzadeh A, Trofimov E A. Additive manufacturing of high entropy alloys: A practical review. *Journal of Materials Science & Technology*, 2021, 77: 131–162
- Cantor B, Chang I T H, Knight P, Vincent A J B. Microstructural development in equiatomic multicomponent alloys. *Materials Science and Engineering: A*, 2004, 375–377: 213–218
- Sathiyamoorthi P, Kim H S. High-entropy alloys with heterogeneous microstructure: processing and mechanical

- properties. *Progress in Materials Science*, 2022, 123: 100709
7. Han C J, Fang Q H, Shi Y S, Tor S B, Chua C K, Zhou K. Recent advances on high-entropy alloys for 3D printing. *Advanced Materials*, 2020, 32(26): 1903855
 8. Yeh J W, Chen S K, Lin S J, Gan J Y, Chin T S, Shun T T, Tsau C H, Chang S Y. Nanostructured high-entropy alloys with multiple principal elements: novel alloy design concepts and outcomes. *Advanced Engineering Materials*, 2004, 6(5): 299–303
 9. McCluskey P J, Vlassak J J. Glass transition and crystallization of amorphous Ni–Ti–Zr thin films by combinatorial nanocalorimetry. *Scripta Materialia*, 2011, 64(3): 264–267
 10. Zhao J C, Xu Y H, Hartmann U. Measurement of an Iso-Curie temperature line of a Co–Cr–Mo solid solution by magnetic force microscopy imaging on a diffusion multiple. *Advanced Engineering Materials*, 2013, 15(5): 321–324
 11. Zheng X, Cahill D G, Weaver R, Zhao J C. Micron-scale measurements of the coefficient of thermal expansion by time-domain probe beam deflection. *Journal of Applied Physics*, 2008, 104(7): 073509
 12. Frazier W E. Metal additive manufacturing: a review. *Journal of Materials Engineering and Performance*, 2014, 23(6): 1917–1928
 13. Saboori A, Gallo D, Biamino S, Fino P, Lombardi M. An overview of additive manufacturing of titanium components by directed energy deposition: microstructure and mechanical properties. *Applied Sciences*, 2017, 7(9): 883
 14. Shi Y S, Yan C Z, Zhou Y, Wu J M, Wang Y, Yu S F, Chen Y. *Materials for Additive Manufacturing*. Cham: Springer, 2021, 379–428
 15. Li B B, Wang B W, Zhu G, Zhang L J, Lu B H. Low-roughness-surface additive manufacturing of metal-wire feeding with small power. *Materials*, 2021, 14(15): 4265
 16. Wang B W, Sun M, Li B B, Zhang L J, Lu B H. Anisotropic response of CoCrFeMnNi high-entropy alloy fabricated by selective laser melting. *Materials*, 2020, 13(24): 5687
 17. Chew Y, Bi G J, Zhu Z G, Ng F L, Weng F, Liu S B, Nai S M L, Lee B Y. Microstructure and enhanced strength of laser aided additive manufactured CoCrFeNiMn high entropy alloy. *Materials Science and Engineering: A*, 2019, 744: 137–144
 18. Kuwabara K, Shiratori H, Fujieda T, Yamanaka K, Koizumi Y, Chiba A. Mechanical and corrosion properties of AlCoCrFeNi high-entropy alloy fabricated with selective electron beam melting. *Additive Manufacturing*, 2018, 23: 264–271
 19. Zhao D D, Yang Q, Wang D W, Yan M, Wang P, Jiang M G, Liu C Y, Diao D F, Lao C S, Chen Z W, Liu Z Y, Wu Y, Lu Z P. Ordered nitrogen complexes overcoming strength–ductility trade-off in an additively manufactured high-entropy alloy. *Virtual and Physical Prototyping*, 2020, 15(sup1): 532–542
 20. Sing S L, Yeong W Y. Laser powder bed fusion for metal additive manufacturing: perspectives on recent developments. *Virtual and Physical Prototyping*, 2020, 15(3): 359–370
 21. Borkar T, Gwalani B, Choudhuri D, Mikler C V, Yannetta C J, Chen X, Ramanujan R V, Styles M J, Gibson M A, Banerjee R. A combinatorial assessment of $Al_xCrCuFeNi_2$ ($0 < x < 1.5$) complex concentrated alloys: microstructure, microhardness, and magnetic properties. *Acta Materialia*, 2016, 116: 63–76
 22. Haase C, Tang F, Wilms M B, Weisheit A, Hallstedt B. Combining thermodynamic modeling and 3D printing of elemental powder blends for high-throughput investigation of high-entropy alloys—towards rapid alloy screening and design. *Materials Science and Engineering: A*, 2017, 688: 180–189
 23. Melia M A, Whetten S R, Puckett R, Jones M, Heiden M J, Argibay N, Kustas A B. High-throughput additive manufacturing and characterization of refractory high entropy alloys. *Applied Materials Today*, 2020, 19: 100560
 24. Chen P, Li S, Zhou Y H, Yan M, Attallah M M. Fabricating CoCrFeMnNi high entropy alloy via selective laser melting *in-situ* alloying. *Journal of Materials Science & Technology*, 2020, 43: 40–43
 25. Chen P, Yang C, Li S, Attallah M M, Yan M. *In-situ* alloyed, oxide-dispersion-strengthened CoCrFeMnNi high entropy alloy fabricated via laser powder bed fusion. *Materials & Design*, 2020, 194: 108966
 26. Li R D, Niu P D, Yuan T C, Cao P, Chen C, Zhou K C. Selective laser melting of an equiatomic CoCrFeMnNi high-entropy alloy: processability, non-equilibrium microstructure and mechanical property. *Journal of Alloys and Compounds*, 2018, 746: 125–134
 27. Brandl E, Heckenberger U, Holzinger V, Buchbinder D. Additive manufactured AlSi10Mg samples using selective laser melting (SLM): microstructure, high cycle fatigue, and fracture behavior. *Materials & Design*, 2012, 34: 159–169
 28. Kenel C, Dasargyri G, Bauer T, Colella A, Spierings A B, Leinenbach C, Wegener K. Selective laser melting of an oxide dispersion strengthened (ODS) γ -TiAl alloy towards production of complex structures. *Materials & Design*, 2017, 134: 81–90
 29. Wei K W, Lv M, Zeng X Y, Xiao Z X, Huang G, Liu M N, Deng J F. Effect of laser remelting on deposition quality, residual stress, microstructure, and mechanical property of selective laser melting processed Ti–5Al–2.5Sn alloy. *Materials Characterization*, 2019, 150: 67–77
 30. Novak T G, Vora H D, Mishra R S, Young M L, Dahotre N B. Synthesis of $Al_{0.5}CoCrCuFeNi$ and $Al_{0.5}CoCrFeMnNi$ high-entropy alloys by laser melting. *Metallurgical and Materials Transactions B*, 2014, 45(5): 1603–1607
 31. Liu Y J, Liu Z, Jiang Y, Wang G W, Yang Y, Zhang L C. Gradient in microstructure and mechanical property of selective laser melted AlSi10Mg. *Journal of Alloys and Compounds*, 2018, 735: 1414–1421
 32. Zheng L J, Liu Y Y, Sun S B, Zhang H. Selective laser melting of Al–8.5Fe–1.3V–1.7Si alloy: Investigation on the resultant microstructure and hardness. *Chinese Journal of Aeronautics*, 2015, 28(2): 564–569
 33. Qiu C L, Wang Z, Aladawi A S, Kindi M A, Hatmi I A, Chen H, Chen L. Influence of laser processing strategy and remelting on surface structure and porosity development during selective laser melting of a metallic material. *Metallurgical and Materials Transactions A*, 2019, 50(9): 4423–4434
 34. Rubenchik A M, King W E, Wu S S. Scaling laws for the additive manufacturing. *Journal of Materials Processing Technology*, 2018, 257: 234–243
 35. AlMangour B, Grzesiak D, Cheng J Q, Ertas Y. Thermal behavior of the molten pool, microstructural evolution, and tribological performance during selective laser melting of TiC/316L stainless

- steel nanocomposites: experimental and simulation methods. *Journal of Materials Processing Technology*, 2018, 257: 288–301
36. Vaidya M, Guruvidyathi K, Murty B S. Phase formation and thermal stability of CoCrFeNi and CoCrFeMnNi equiatomic high entropy alloys. *Journal of Alloys and Compounds*, 2019, 774: 856–864
 37. Vaidya M, Pradeep K G, Murty B S, Wilde G, Divinski S V. Bulk tracer diffusion in CoCrFeNi and CoCrFeMnNi high entropy alloys. *Acta Materialia*, 2018, 146: 211–224
 38. Wang Y M, Voisin T, McKeown J T, Ye J C, Calta N P, Li Z, Zeng Z, Zhang Y, Chen W, Roehling T T, Ott R T, Santala M K, Depond P J, Matthews M J, Hamza A V, Zhu T. Additively manufactured hierarchical stainless steels with high strength and ductility. *Nature Materials*, 2018, 17(1): 63–71
 39. Zhu Z G, Nguyen Q B, Ng F L, An X H, Liao X Z, Liaw P K, Nai S M L, Wei J. Hierarchical microstructure and strengthening mechanisms of a CoCrFeNiMn high entropy alloy additively manufactured by selective laser melting. *Scripta Materialia*, 2018, 154: 20–24
 40. Bhattacharjee P P, Sathiaraj G D, Zaid M, Gatti J R, Lee C, Tsai C W, Yeh J W. Microstructure and texture evolution during annealing of equiatomic CoCrFeMnNi high-entropy alloy. *Journal of Alloys and Compounds*, 2014, 587: 544–552
 41. Ni M, Chen C, Wang X J, Wang P W, Li R D, Zhang X Y, Zhou K C. Anisotropic tensile behavior of *in situ* precipitation strengthened Inconel 718 fabricated by additive manufacturing. *Materials Science and Engineering: A*, 2017, 701: 344–351
 42. Wan H Y, Zhou Z J, Li C P, Chen G F, Zhang G P. Effect of scanning strategy on grain structure and crystallographic texture of Inconel 718 processed by selective laser melting. *Journal of Materials Science & Technology*, 2018, 34(10): 1799–1804
 43. Sun S J, Tian Y Z, Lin H R, Dong X G, Wang Y H, Zhang Z J, Zhang Z F. Enhanced strength and ductility of bulk CoCrFeMnNi high entropy alloy having fully recrystallized ultrafine-grained structure. *Materials & Design*, 2017, 133: 122–127
 44. Laplanche G, Kostka A, Horst O M, Eggeler G, George E P. Microstructure evolution and critical stress for twinning in the CrMnFeCoNi high-entropy alloy. *Acta Materialia*, 2016, 118: 152–163
 45. Jang M J, Joo S H, Tsai C W, Yeh J W, Kim H S. Compressive deformation behavior of CrMnFeCoNi high-entropy alloy. *Metals and Materials International*, 2016, 22(6): 982–986
 46. Gludovatz B, George E P, Ritchie R O. Processing, microstructure and mechanical properties of the CrMnFeCoNi high-entropy alloy. *JOM*, 2015, 67(10): 2262–2270
 47. Lin Q Y, An X H, Liu H W, Tang Q H, Dai P Q, Liao X Z. *In-situ* high-resolution transmission electron microscopy investigation of grain boundary dislocation activities in a nanocrystalline CrMnFeCoNi high-entropy alloy. *Journal of Alloys and Compounds*, 2017, 709: 802–807
 48. Prashanth K G, Eckert J. Formation of metastable cellular microstructures in selective laser melted alloys. *Journal of Alloys and Compounds*, 2017, 707: 27–34
 49. Voisin T, Forien J B, Perron A, Aubry S, Bertin N, Samanta A, Baker A, Wang Y M. New insights on cellular structures strengthening mechanisms and thermal stability of an austenitic stainless steel fabricated by laser powder-bed-fusion. *Acta Materialia*, 2021, 203: 116476
 50. Tong Z P, Ren X D, Jiao J F, Zhou W F, Ren Y P, Ye Y X, Larson E A, Gu J Y. Laser additive manufacturing of FeCrCoMnNi high-entropy alloy: Effect of heat treatment on microstructure, residual stress and mechanical property. *Journal of Alloys and Compounds*, 2019, 785: 1144–1159
 51. Wu Z, David S A, Leonard D N, Feng Z, Bei H. Microstructures and mechanical properties of a welded CoCrFeMnNi high-entropy alloy. *Science and Technology of Welding and Joining*, 2018, 23(7): 585–595